RSC Applied Polymers

PAPER

View Article Online
View Journal

Cite this: DOI: 10.1039/d6lp00158k

Tailored surface modification of cellulose nanofibers enables enhanced co-adsorption of nanoplastics and mercury ions

Zhichun Liu,[a] Haijun Yu,[a] Lu Bai[b] and Zhicheng Liu*[a]

Addressing the challenge of simultaneous removal of disparate pollutants like nanoplastics (NPs) and heavy metal ions (Hg^{2+}), we developed a bifunctional cellulose nanofibrous membrane *via* electrospinning followed by targeted surface modification. Material characterization confirmed the intended structural and chemical features. Adsorption kinetics fit the pseudo-second-order model, while equilibrium data aligned with the Langmuir model, yielding maximum capacities of 47.6 mg g^{-1} for NPs and 65.2 mg g^{-1} for Hg^{2+}. Thermodynamic analysis indicated spontaneous and endothermic chemisorption processes. XPS and DFT calculations provided detailed mechanistic insights, identifying quaternary ammonium sites as crucial for NP binding (electrostatic interaction, H-bonding) and C–S–C, $-NH_2$, and –COOH groups, particularly the engineered C–S–C linkage, as key chelating sites for Hg^{2+}. Significantly, a unique synergistic bridging mechanism was discovered during simultaneous adsorption: Hg^{2+} reduced NP surface charge, enabling layered stacking, while NPs facilitated Hg^{2+} uptake *via* platform bridging, enhancing removal efficiency beyond single-pollutant scenarios. These findings highlight complex interactions in multi-component adsorption systems and offer avenues for designing efficient multifunctional materials.

Received 28th April 2026,
Accepted 18th June 2026

DOI: 10.1039/d6lp00158k

rsc.li/rscapplpolym

1 Introduction

Water pollution represents a major environmental challenge in contemporary society, with the diversity and complexity of pollution sources continuously exacerbating environmental and health risks.[1–4] Among various traditional pollutants, heavy metal ions are highly toxic, bioaccumulative, and non-degradable.[5,6] They can enter the human body through drinking water, aquatic organisms, and other pathways, accumulating along the food chain. Long-term exposure may lead to neurotoxicity, renal dysfunction, developmental abnormalities, and even various cancers.[7] Meanwhile, microplastics (MPs) and nanoplastics (NPs), as emerging contaminants with wider distribution,[8,9] have gradually revealed extensive yet hidden threats to ecosystems and human health. They are not only resistant to degradation but can also penetrate into cells, triggering oxidative stress, inflammatory responses, mitochondrial damage, and genetic material disruption.[10–14] Even more concerning, these MPs and NPs can act as carriers that adsorb heavy metals, persistent organic pollutants, and other contaminants, forming composite pollution and enhancing their bioavailability and transportability.[15,16] Confronted with the complex scenario involving the coexistence of traditional and emerging pollutants, the development of efficient, synergistic, and sustainable control technologies has become an urgent and challenging task in the field of environmental remediation.[17]

Among various pollutant treatment methods, adsorption is widely adopted due to its high efficiency, operational simplicity, and broad applicability. For the removal of heavy metals, numerous adsorbent materials have been developed to date. These materials often achieve efficient and selective adsorption through functionalization with strong complexing groups that form stable coordination bonds with metal ions or facilitate ion exchange.[18–20] For instance, Ji *et al.*[21] grafted thioglycolic acid onto MOF-808, utilizing the –SH groups in the thiol-functionalized MOF-808 as key adsorption sites to achieve specific inner-sphere coordination with Hg(II), enabling highly selective removal. As for the removal of MPs and NPs, various adsorbents including carbon materials, nanofibers, MOFs, and hydrogels were prepared. These adsorbents could form favorable interactions such as electrostatic interactions,[22] surface complexation,[23] hydrophobic interactions,[24] and hydrogen bonding[25] with MPs or NPs to improve adsorption capacity.[26] For example, Wang *et al.*[27] synthesized a composite aerogel using oxidized cellulose nanofibers as the matrix and flash graphene as the modifier. This material achieves effective removal of MPs from aquatic environments through hydrophobic interaction, pore-

[a]*School of Materials Science and Engineering, Ocean University of China, Qingdao, 266100, China. E-mail: zcliu@ouc.edu.cn*
[b]*Institute for Chemical Biology & Biosensing, College of Life Sciences, Qingdao University, Qingdao, 266071, China*

filling effect, capillary force, and electrostatic interaction. Notably, most of the adsorbents are designed for single-pollutant removal. In real water environments where multiple contaminants coexist, their adsorption performance can be significantly compromised, particularly due to competitive adsorption or mutual interference among different pollutants.[28] Therefore, developing multifunctional adsorbent materials capable of simultaneously and efficiently removing various types of pollutants has become a crucial and urgent challenge in the field of water pollution control.

In this work, we have developed a novel cellulose nanofiber membrane with customized functional groups for the simultaneous removal of NPs and Hg^{2+}. Initially, cellulose nanofibrous membranes were prepared through electrospinning, followed by sequential grafting using 2,3-epoxypropyltrimethylammonium chloride (GTA) and L-cysteine (L-Cys) to produce bifunctionalized cellulose nanofibrous membranes (DCAF-GTA-Cys). Then, the morphology and structural properties of DCAF-GTA-Cys were characterized using scanning electron microscopy, Fourier transform infrared spectroscopy, zeta potential, water contact angle, and tensile tests. We also investigated the adsorption behaviors of this material for NPs and Hg^{2+} under varying conditions, including pH, contact time, adsorption temperature, initial concentration, and the influence of co-existing ions. To understand the underlying mechanisms, we utilized XPS in conjunction with theoretical computations. It is hypothesized that the bifunctional cellulose nanofibers could demonstrate routine adsorption performance toward the contaminants. Unexpectedly, unlike the conventional competitive adsorption mechanism, we found that the adsorbent exhibited enhanced adsorptive properties due to an intriguing bridging effect arising from the coexistence of pollutants. These findings may offer a new solution for developing environmentally friendly, efficient, multifunctional, and cost-effective adsorbent materials.

2 Experimental section

2.1 Chemicals and reagents

Cellulose acetate (CA, with an acetyl content of 39.8 wt%) and L-cysteine (L-Cys, 99%) were obtained from Aladdin Biochemical Science and Technology Co. A range of analytical reagents such as acetone and *N*,*N*-dimethylacetamide (DMAc) was used. Other reagents with analytical reagent grade were sourced from Sinopharm Chemical Reagent Co. and included: hydrochloric acid (HCl), sulfuric acid (H_2SO_4), metal salts (Na_2SO_4, NaCl, $NaHCO_3$, Na_3PO_4, Na_2CO_3, $CaCl_2$, KCl, $AlCl_3$), and sodium hydroxide (NaOH). Additionally, 2,3-epoxypropyltrimethylammonium chloride (GTA, 95%) and glutaraldehyde (GA, 25%) were provided by Shanghai McLean Biochemistry Science and Technology Co. Ltd. Sodium nitrate ($NaNO_3$, 99%) came from Xilong Science Co. Ltd, and mercuric chloride standard solution ($HgCl_2$, 1000 μg mL^{-1}) was supplied by Beijing Beiweiyi Measurement and Technology Institute. The 50 nm green fluorescence-labelled carboxylated polystyrene nanospheres from Shanghai Yiyuan Biotechnology Co. were utilized as model NPs.

2.2 Preparation of adsorbents

Electrospinning was employed to create cellulose acetate nanofibers (CAF).[29] Initially, a homogeneous mixture was prepared by dissolving CA (2.92 g) in a solvent system composed of acetone and DMAc (in a 2 : 1 ratio) and agitating it for 12 hours. The electrospinning procedure utilized a high voltage (11.5 kV), and was conducted over a 12-hour span with a relative humidity range of 40% to 50%. The distance between the spinneret and the drum collector was 15 cm, and a solution flow rate of 0.6 mL h^{-1} was used. Subsequently, regenerated cellulose nanofibrous membranes (DCAF) were produced through deacetylation in 0.1 M NaOH solution for one day.

For modification, 0.1 g of DCAF, 0.59 g of NaOH, and 0.4 g of GTA were dissolved in 13 mL of deionized water, and the mixture was subjected to ultrasonication for 30 minutes. The reaction proceeded for 5 hours at 50 °C. Post-reaction, the GTA-modified DCAF membrane (DCAF-GTA) was washed with deionized water and vacuum-dried at 60 °C for 6 hours. Next, 0.1 g of DCAF-GTA was dissolved with 0.1 g of L-Cys in 30 mL of deionized water, followed by the addition of 2 mL of GA. The reaction was carried out for 3 hours at 35 °C. Finally, the membrane was washed and vacuum-dried to yield the bifunctionalized DCAF-GTA-Cys membrane.

2.3 Characterization

The detailed characterizations such as scanning electron microscopy and Fourier transform infrared spectroscopy could be found in the SI.

2.4 Adsorption experiment

All adsorption experiments were conducted in 50 mL glass vials, which were placed on a shaker set at 150 rpm and maintained at 25 °C. All relevant adsorption experiments were performed 3 times. A fixed amount of adsorbent was introduced into solutions containing either NPs, Hg^{2+} ions, or a combination of both, yielding samples labeled as DCAF-GTA-Cys-NPs, DCAF-GTA-Cys-Hg^{2+} and DCAF-GTA-Cys-NPs & Hg^{2+}, respectively. After the adsorption, the residual concentration of the NPs (Fig. S1) was measured using fluorescence spectrophotometer (Hitachi F-7000), while Hg^{2+} concentration was determined *via* inductively coupled plasma optical emission spectroscopy (ICP-OES, Agilent 725). The adsorption characteristics were examined through kinetics, isotherm models, and thermodynamic analyses, along with an investigation into the influence of co-existing ions on the adsorption process. Further details of the experiments are available in the SI.

2.5 Theoretical calculation

To elucidate the specific adsorption sites involved, theoretical calculations were employed to examine the adsorption behavior of both NPs and Hg^{2+} ions onto DCAF-GTA-Cys. These simulation details can be found in the SI.

3 Results and discussion

3.1 Structural characterizations

The preparation of bifunctionalized cellulose nanofibrous membranes involves a simple electrospinning process followed by sequential modifications, as detailed in Fig. 1. The whole process can be summarized as follows: initially, cellulose acetate nanofibrous membranes were produced using electrospinning. These membranes were then converted to regenerated cellulose nanofibrous membranes through a deacetylation process. Quaternary ammonium groups were introduced to the fibrous membranes through GTA grafting. This modification enhances the cationic properties of the cellulose membranes, thereby increasing their ability to adsorb negatively charged NPs. In the final modification step, various functional groups, including C–S–C, $-NH_2$, –COOH, and hydroxyl groups, were introduced to the membrane surface by grafting L-Cys. These groups could form coordination bonds with Hg^{2+}, significantly improving the adsorption of heavy metal ions. The synergistic effect of adsorbing both NPs and Hg^{2+} could be achieved through the strategic introduction of different chemical functional groups, enhancing the overall adsorption performance of the membranes.

The morphology of the nanofiber membrane is closely related to its surface area and pore structure, impacting the number and distribution of adsorption sites and thus the adsorption effectiveness. Fig. 2 illustrates the morphological changes before and after the modifications. It was observed

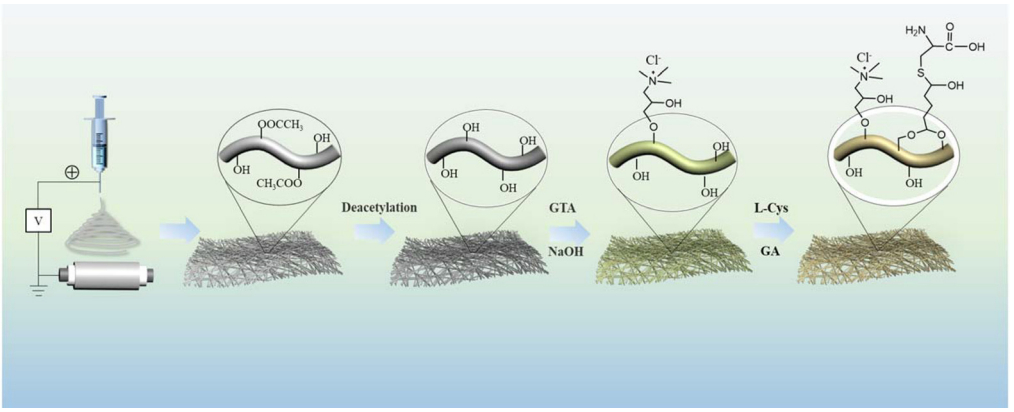

Fig. 1 Schematic diagram of the preparation process of DCAF-GTA-Cys.

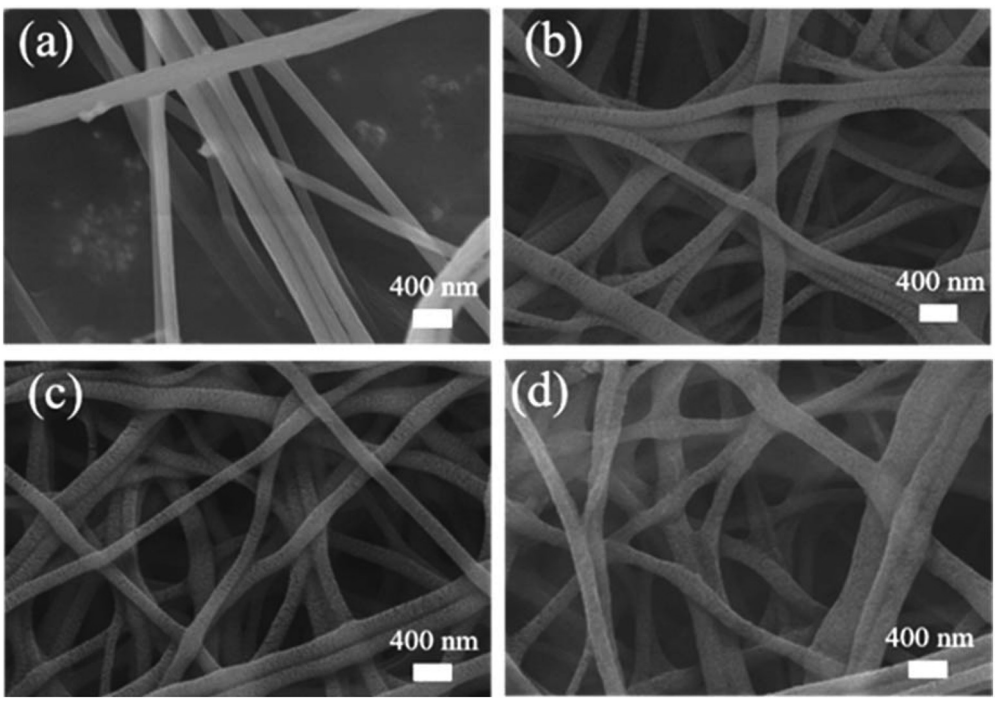

Fig. 2 SEM images of (a) CAF, (b) DCAF, (c) DCAF-GTA, and (d) DCAF-GTA-Cys.

that the treatment with GTA induced distinct structural changes in the DCAF fibers. This is likely because the epoxy groups of GTA react with hydroxyl groups on cellulose, consuming a portion of the hydroxyl groups. Such consumption disrupts the original hydrogen bond network between cellulose molecules, leading to a looser fiber structure. Additionally, the deacetylation process itself may also contribute to this structural change.[30] Following L-Cys modification, cross-linking mediated by GA further contributed to the structural alteration, while the overall spatial architecture of the membrane remained well-maintained.

FTIR analysis was used to examine the changes in functional groups before and after modification. As shown in Fig. 3, the surface chemical structures of the membranes at each modification stage were well-resolved. Compared with the pristine DCAF, several new features appeared in the spectrum of DCAF-GTA. The newly emerged peaks at 772 cm^{-1} and 1469 cm^{-1} are assigned to the bending vibration of the C–N bond[31] and the bending vibration of the C–H bond from the GTA,[32] respectively. Moreover, the broadening of the absorption band around 2900 cm^{-1} indicates the successful incorporation of the alkyl methyl groups from GTA into the cellulose matrix. Crucially, the successful grafting of GTA *via* the chemical reaction with surface hydroxyl groups of cellulose is evidenced by the status of the epoxy ring. Owing to the significant thermodynamic ring strain of the three-membered oxirane ring, the epoxy group of GTA is highly reactive and readily undergoes nucleophilic ring-opening when attacked by the surface –OH groups under reaction conditions. Consequently, the typical sharp characteristic peaks of free epoxy groups—usually expected around 1257 cm^{-1} (symmetric ring stretching) and 810–950 cm^{-1} (asymmetric ring stretching)—were absent in the DCAF-GTA spectrum, confirming the successful ring-opening covalent attachment.[33,34] After L-Cys modification, two new peaks appeared at 1590 cm^{-1} and 1714 cm^{-1} in DCAF-GTA-Cys, associated with the bending vibrations of the amino N–H bond and the stretching vibrations of the carboxyl C=O bond in L-Cys.[35,36] The absence of the peak around 2600 cm^{-1}, typically indicative of –SH groups, implies their conversion to C–S–C bonds. Thus, the L-Cys molecule was effectively grafted onto DCAF-GTA, resulting in the formation of DCAF-GTA-Cys.

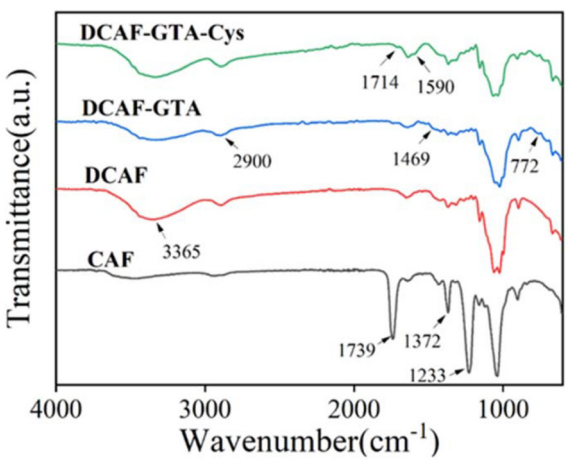

Fig. 3 FTIR spectra of CAF, DCAF, DCAF-GTA and DCAF-GTA-Cys.

It is well established that the hydrophilicity, mechanical properties, and surface charge characteristics of an adsorbent significantly influence its adsorption performance. To determine the hydrophilicity, we examined the water contact angles of the cellulose nanofiber membranes before and after modification (Fig. 4a and b). Initially, the water contact angle of the CAF membrane was 116°, which decreased to 13.6° after modification. This change is likely due to alterations in the functional groups on the surface of the nanofiber membrane. Prior to modification, the surface hydroxyl groups of CAF were esterified with acetic acid, imparting a degree of hydrophobicity to the membrane. After modification, these esterified hydroxyl groups were exposed and grafted with other functional groups. Specifically, GTA introduced polar quaternary ammonium groups, while L-Cys added amino ($-NH_2$) and carboxyl (–COOH) groups. These additional polar groups strengthened surface polarity, promoting stronger interactions with water molecules.[37] The reduction in water contact angle could facilitate more effective contact with pollutants in aqueous environments and improve the adsorption process.

Analysis of the stress–strain curves reveals (Fig. 4c) that the elongation at break for the nanofiber membrane prior to modification was approximately 38%, indicating considerable toughness. Post-modification, however, the elongation at break decreased to around 7%, although the tensile strength significantly increased. This change can be attributed to two factors: firstly, the increase in hydroxyl groups due to deacetylation enhances hydrogen bonding, and secondly, the use of GA in the modification process crosslinks some cellulose molecules, thereby increasing tensile strength while reducing toughness. Despite the decrease in toughness, the modified DCAF-GTA-Cys remains effective as an adsorbent. The increased strength allows the fibrous membrane to retain its structure during water impact, which benefits both the pollutant adsorption process and the recovery of the adsorbent.

The zeta potential result illustrates the surface charge characteristics of the adsorbent and the model NPs across various pH levels. In the pH range of 3–10 (Fig. 4d), DCAF-GTA-Cys exhibits a positive zeta potential, indicating a positively charged surface, whereas the NPs show negative zeta potentials, signifying a negatively charged surface. Thus, an electrostatic interaction between the positively charged DCAF-GTA-Cys and the negatively charged NPs could occur, facilitating the removal process.

3.2 Adsorption performance

The morphology of the membrane following adsorption provides clear evidence of the effectiveness of the adsorbent. When NPs were adsorbed (Fig. 5a), a tightly packed arrangement of NPs was observed on the nanofiber surface with no noticeable agglomeration, which can be attributed to the electrostatic repulsion generated by the negative charges on

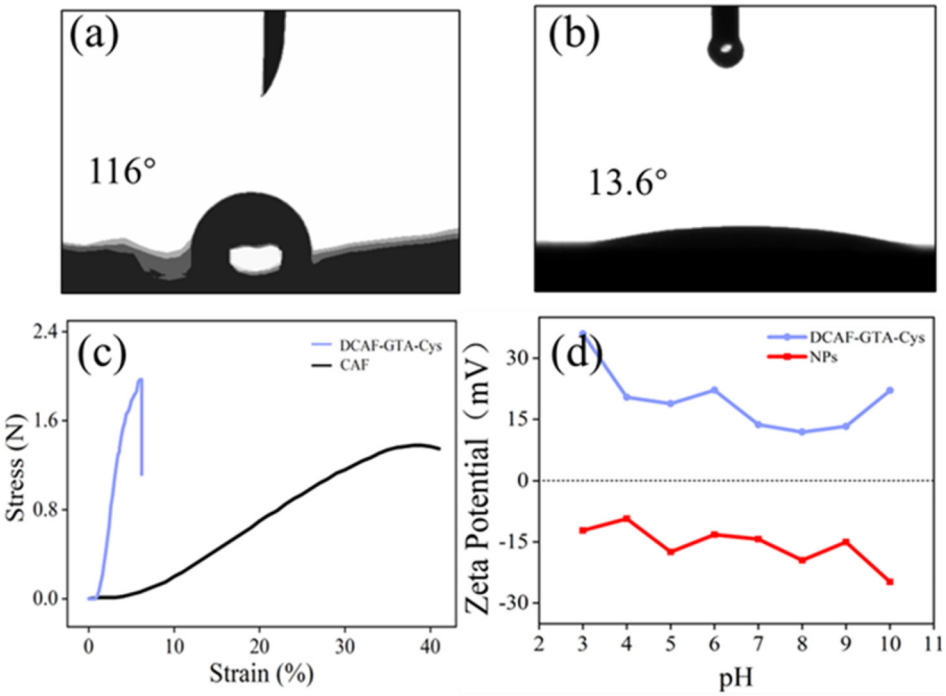

Fig. 4 Water contact angle images of (a) CAF and (b) DCAF-GTA-Cys. (c) Stress–strain curves of CAF and DCAF-GTA-Cys. (d) The zeta potentials of NPs and DCAF-GTA-Cys at different pH.

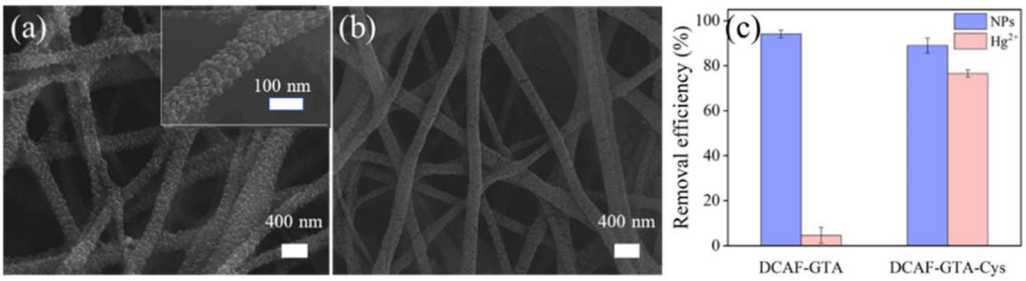

Fig. 5 SEM images of (a) DCAF-GTA-Cys-NPs, (b) DCAF-GTA-Cys-Hg^{2+}, (c) comparison of the removal efficiencies of the pollutants by DCAF-GTA and DCAF-GTA-Cys membranes.

the immobilized NPs that prevented their aggregation. When the DCAF-GTA-Cys membrane was used for the adsorption of Hg^{2+} (Fig. 5b), the morphology of the nanofibers remained largely unchanged.

In order to demonstrate the necessity of introducing customized functional groups through sequential grafting, we used DCAF-GTA and DCAF-GTA-Cys to separately adsorb NPs and Hg^{2+} (Fig. 5c). The results indicated that DCAF-GTA, grafted only with GTA, exhibited high removal efficiency for NPs but had minimal effect on Hg^{2+}. In contrast, DCAF-GTA-Cys, modified with both GTA and L-Cys, not only maintained excellent removal efficiency for NPs but also significantly removed Hg^{2+}. These findings not only confirm the successful modification of DCAF-GTA with L-Cys, but also highlight the presence of effective Hg^{2+} adsorption sites provided by L-Cys. The elaborate modification strategy notably endows the nanofiber membrane with dual adsorption capacity for target pollutants.

Studying adsorption kinetics is essential for understanding the rate and mechanism of adsorption. We investigated the effect of adsorption time on the uptake of NPs and Hg^{2+} (Fig. 6a and b). Fig. 6a illustrates that adsorption increases over time, which can be divided into three phases: (1) surface adsorption during the first 720 minutes, where rapid adsorption primarily occurs on the surface of DCAF-GTA-Cys; (2) internal diffusion from 720 to 1440 minutes, where adsorption growth is controlled by the diffusion rate of NPs into the nanofiber membrane; and (3) an equilibrium phase after 1440 minutes, where adsorption and desorption reach equilibrium. Fig. 6b shows a similar trend for Hg^{2+}, with an initial rapid increase in adsorption during the first 8 minutes, pri-

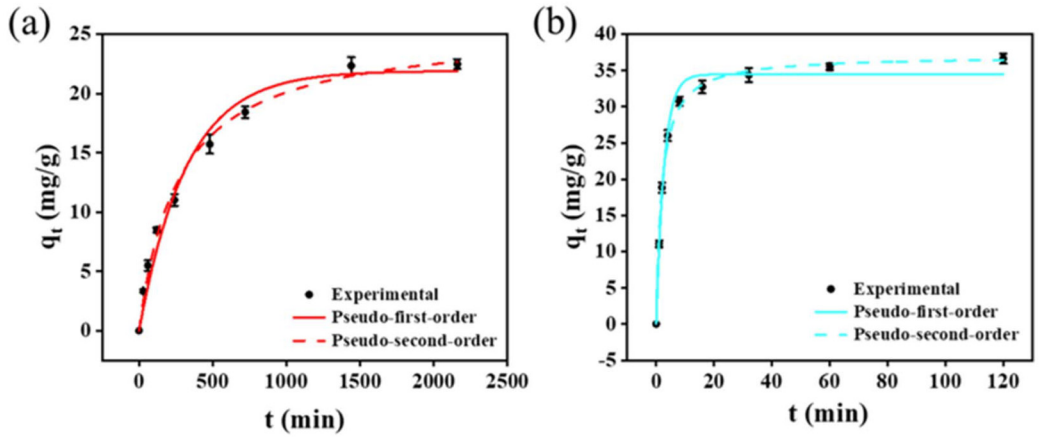

Fig. 6 Adsorption kinetics of DCAF-GTA-Cys on NPs (a) and Hg^{2+} (b).

marily on the surface of the nanofiber membrane. From 8 to 32 minutes, Hg^{2+} diffuses into the nanofiber interior, and by 32 minutes, the adsorption–desorption reaction reaches equilibrium due to the saturation of Hg^{2+} adsorption sites on the DCAF-GTA-Cys surface.

We fitted the adsorption data of NPs and Hg^{2+} on DCAF-GTA-Cys using both pseudo-first-order and pseudo-second-order kinetic models. For NPs, the pseudo-second-order model better fits the experimental data, with an R^2 value of 0.99, higher than the pseudo-first-order model's R^2 value of 0.97. The predicted adsorption amount closely aligns with the experimental result (Fig. 6a and Table S1). Similarly, for Hg^{2+}, the pseudo-second-order model was more accurate (Fig. 6b and Table S1) with an R^2 value of 0.99, and the predicted adsorption value more closely matched the experimental result. These findings suggest that the adsorption of NPs and Hg^{2+} on DCAF-GTA-Cys is dominated by chemisorption processes.

The investigation of adsorption isotherms allows the determination of the equilibrium adsorption amount at varying concentrations, thereby elucidating the adsorption capacity and affinity. We varied the initial concentrations to measure the equilibrium adsorption amounts of NPs and Hg^{2+} (Fig. 7a and c). For NPs, adsorption increased with initial NPs concentrations below 70 mg L^{-1}, reaching saturation at about 70 mg L^{-1} with a peak adsorption of 47.6 mg g^{-1}. Similarly, Hg^{2+} adsorption grew with initial Hg^{2+} concentrations up to 100 mg L^{-1}, beyond which adsorption sites were fully occupied, capping at 65.2 mg g^{-1}.

To explore the adsorption behavior of the pollutants on the nanofiber membrane, we analyzed the data using the well-known Langmuir and Freundlich models.[38] The adsorption process of NPs and Hg^{2+} both fitted well with the Langmuir model (Fig. 7b and d), with R^2 values of 0.98 and 0.99 (Table S2), respectively. Additionally, the Langmuir model's predicted maximum adsorption capacity closely matches the experimental values, indicating that the adsorption of NPs and Hg^{2+} by DCAF-GTA-Cys follows to monolayer adsorption characteristics.

By analyzing adsorption thermodynamics, we can determine the thermal effects and the spontaneity of the adsorption process. We investigated the effect of temperature on the adsorption of NPs and Hg^{2+} (Fig. 8a–d). For DCAF-GTA-Cys in the adsorption of NPs and Hg^{2+}, the amount of adsorbed adsorbates increased with rising temperature, suggesting endothermic reactions. The positive value of ΔH indicates that higher temperatures enhance the adsorption of both NPs and Hg^{2+} by DCAF-GTA-Cys (Table S3), while the negative value of ΔG confirms the spontaneity of the adsorption processes. This can be attributed to the fact that higher temperatures accelerate molecular motion and facilitate the diffusion of the pollutants into the nanofiber membrane.

The presence of other ions would interfere with or compete with the adsorption of the target substances in practical applications. Regarding the effect of co-existing anions on the removal efficiency of NPs (Fig. 9a), ions such as Cl^-, CO_3^{2-}, and NO_3^- showed slight inhibitory effects, with changes in removal efficiency within 15%. Moreover, the effect of various co-existing cations on Hg^{2+} removal efficiency was studied (Fig. 9b). The removal efficiency of Hg^{2+} dropped by approximately 5% with the addition of Mg^{2+}, which may be attributed to competitive adsorption between Mg^{2+} and Hg^{2+}. Other ions such as Ca^{2+}, Na^+, K^+, and Al^{3+} had a lesser impact on Hg^{2+} removal, indicating that DCAF-GTA-Cys exhibits a certain selectivity in its adsorption of Hg^{2+}. In addition, we evaluated the recyclability of DCAF-GTA-Cys for Hg^{2+} removal through five consecutive adsorption–desorption cycles using dilute hydrochloric acid as the eluent. As shown in Fig. S4, although a slight decline in the removal efficiency was observed after repeated cycles, the membrane maintained a substantial portion of its initial capacity, highlighting its excellent regenerability and cost-effective potential for practical water purification.

Overall, the DCAF-GTA-Cys adsorbent exhibits comparable and competitive adsorption capacities toward both NPs and Hg^{2+} relative to previously reported advanced adsorbents (Table S4). It is worth noting that while the absolute Hg^{2+}

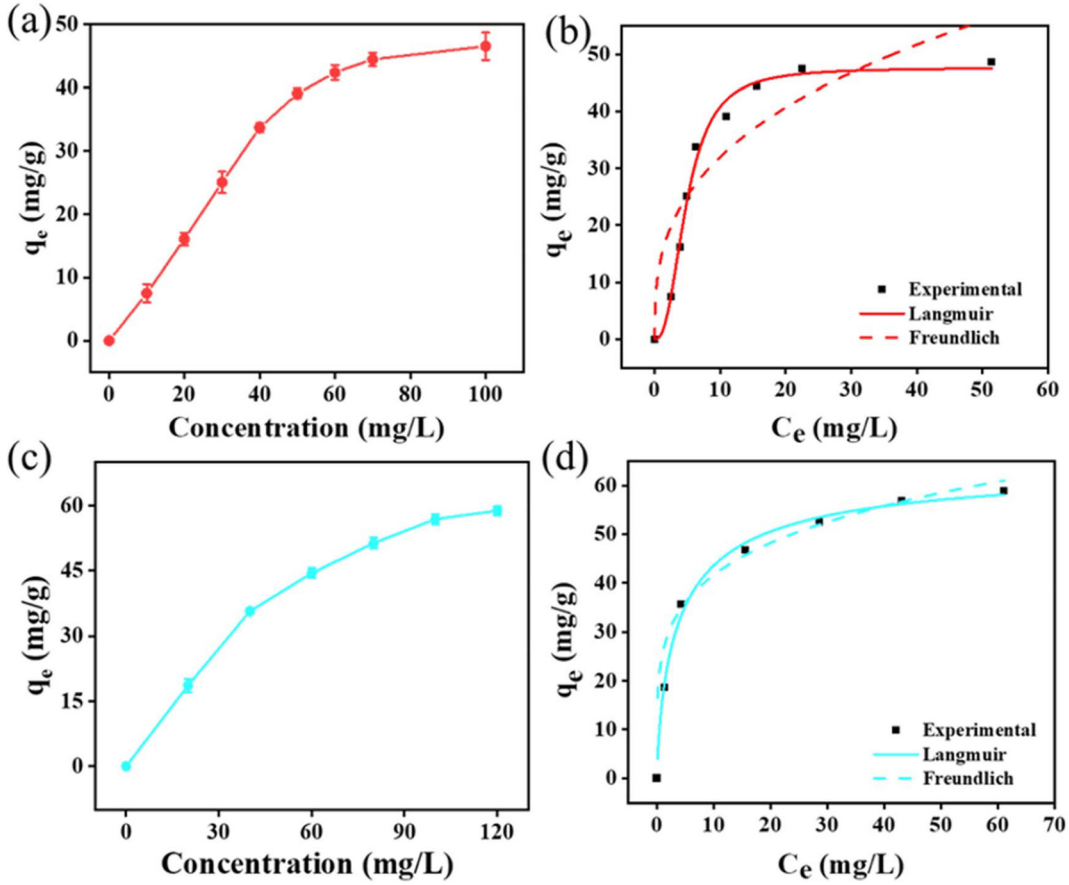

Fig. 7 Effect of initial concentration on the adsorption of NPs (a) and Hg^{2+} (c) by DCAF-GTA-Cys. Adsorption isotherms for DCAF-GTA-Cys adsorption of NPs (b) and Hg^{2+} (d).

capacity is moderate, our material provides a balanced and sustainable alternative. The distinctive competitiveness of DCAF-GTA-Cys lies in its eco-friendly cellulose matrix, excellent structural integrity for easy recycling, and crucially, its bifunctional removal capability for complex pollutants.

Given the bifunctional design of our engineered adsorbent, we anticipate effective removal of multiple coexisting pollutants. In a recent work, Li *et al.* synthesized a composite material impregnated with biochar to improve the adsorption capacity for various pollutants, including ciprofloxacin (CIP) and roxarsone (ROX).[39] This material effectively removes multiple contaminants primarily through different interactions such as hydrogen bonding and electrostatic interactions. However, when both CIP and ROX are present together, competitive adsorption occurs, leading to a reduction in the overall efficiency of the adsorption process.

Unexpectedly, we observed an interesting bridging effect in the simultaneous removal of NPs and Hg^{2+} by DCAF-GTA-Cys. During simultaneous adsorption of NPs and Hg^{2+} (Fig. S2), polystyrene nanospheres covered the nanofiber surfaces, exhibiting a characteristic "ball-on-ball" stacking pattern, in contrast to the previously observed monolayer NP adsorption. This phenomenon can be explained by the interaction of Hg^{2+} with carboxyl groups on the NPs surface, which reduces the charge on the NPs,[40] thus weakening the repulsive forces between individual NPs. To provide more evidence for the hypothesized mechanism, zeta potential measurements of the NPs were conducted in the presence of varying Hg^{2+} concentrations prior to their contact with the adsorbent (Fig. S5). The zeta potential of the NPs shifted toward zero upon increasing Hg^{2+} concentration. This evident charge-neutralization confirms the Hg^{2+}–carboxylate interactions, which effectively suppresses inter-particle electrostatic repulsion and directly triggers the subsequent synergistic bridging effect. Furthermore, Hg^{2+} ions serve as bridging agents, facilitating the formation of NP aggregates through a bridging mechanism, which promotes the sequential deposition of additional NPs onto previously adsorbed particles.

To further validate this special adsorption behavior, we varied the concentration of one target pollutant in solution and recorded its impact on the adsorption of the other (Fig. 10a and b). The results show that the presence of Hg^{2+} in solution enhances the adsorption of NPs by DCAF-GTA-Cys, while the presence of NPs promotes the adsorption of Hg^{2+}, demonstrating a mutual and synergistic adsorption effect.

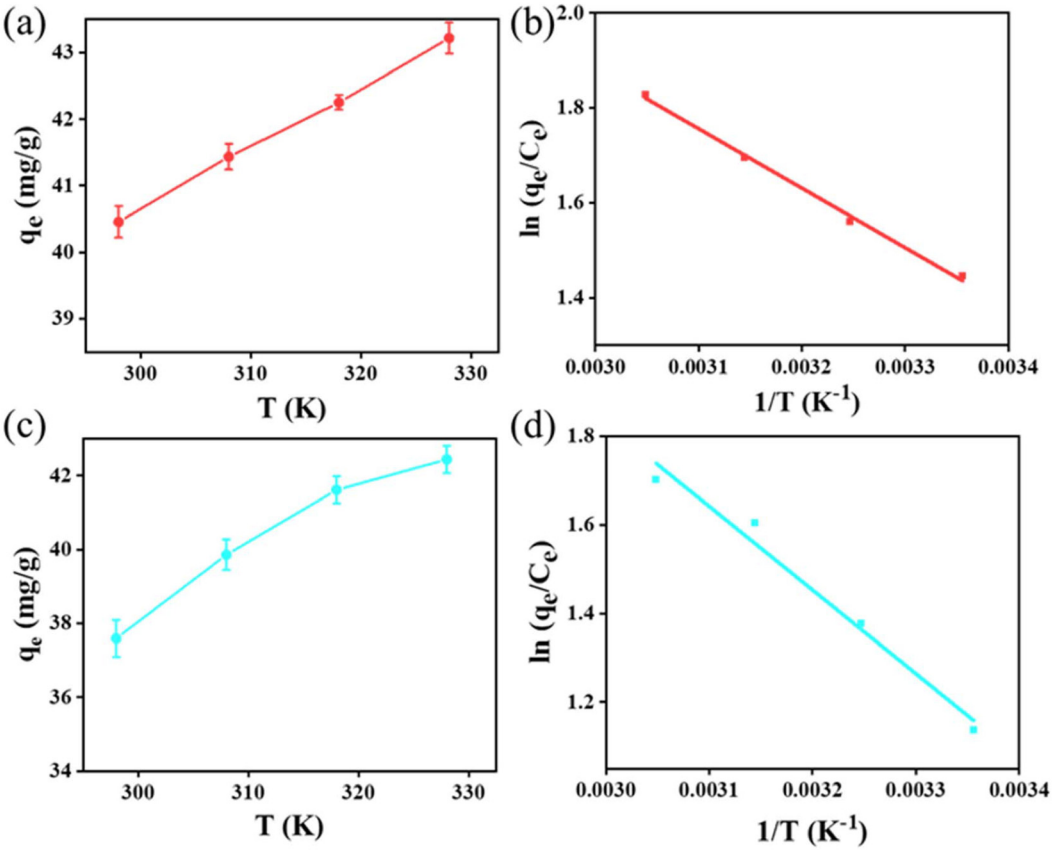

Fig. 8 Effect of temperature on the adsorption of NPs (a) and Hg^{2+} (c) by DCAF-GTA-Cys. Thermodynamics fitting of adsorption towards NPs (b) and Hg^{2+} (d) by DCAF-GTA-Cys.

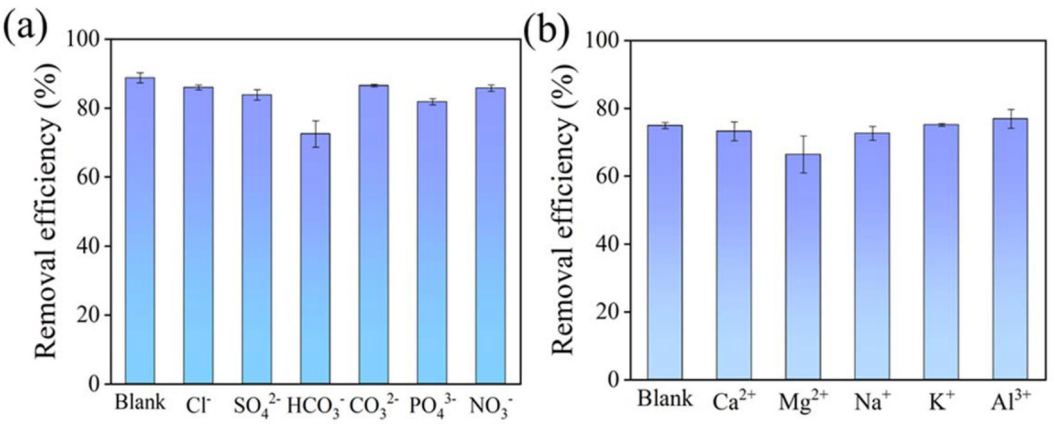

Fig. 9 Effect of different ions on the adsorption of NPs (a) and Hg^{2+} (b) by DCAF-GTA-Cys.

This result further confirms a weak but notable interaction between NPs and Hg^{2+}. The enhanced adsorption of NPs may be attributed to a divalent ion bridging effect,[28] wherein Hg^{2+} ions act as linkers connecting the NPs to the DCAF-GTA-Cys substrate, thus promoting NP deposition. Conversely, the increased uptake of Hg^{2+} could result from the NPs themselves serving as bridging platforms, facilitating greater Hg^{2+} adsorption onto the material. This synergistic behavior suggests the formation of layered complex structures, potentially arranged as either DCAF-GTA-Cys–NPs–Hg^{2+}–NPs or DCAF-GTA-Cys–Hg^{2+}–NPs–Hg^{2+}, accounting for the mutual enhancement of adsorption (Fig. 11).

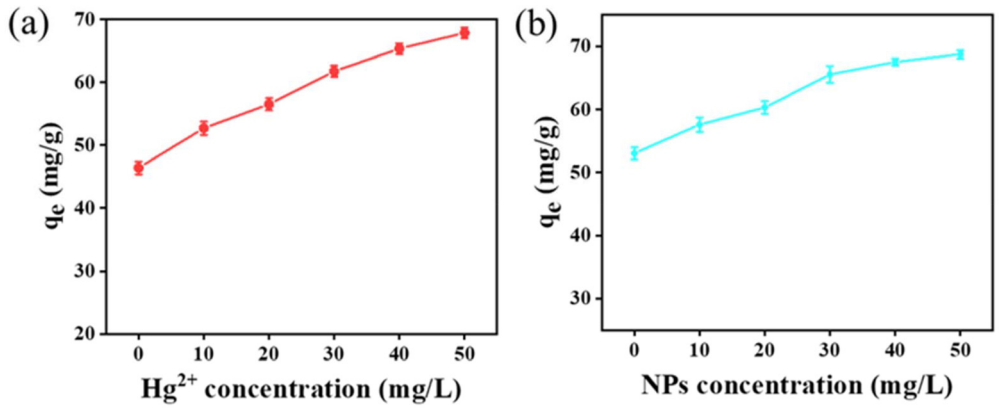

Fig. 10 (a) Effect of Hg^{2+} on the adsorption of NPs by DCAF-GTA-Cys; (b) effect of NPs on the adsorption of Hg^{2+} by DCAF-GTA-Cys.

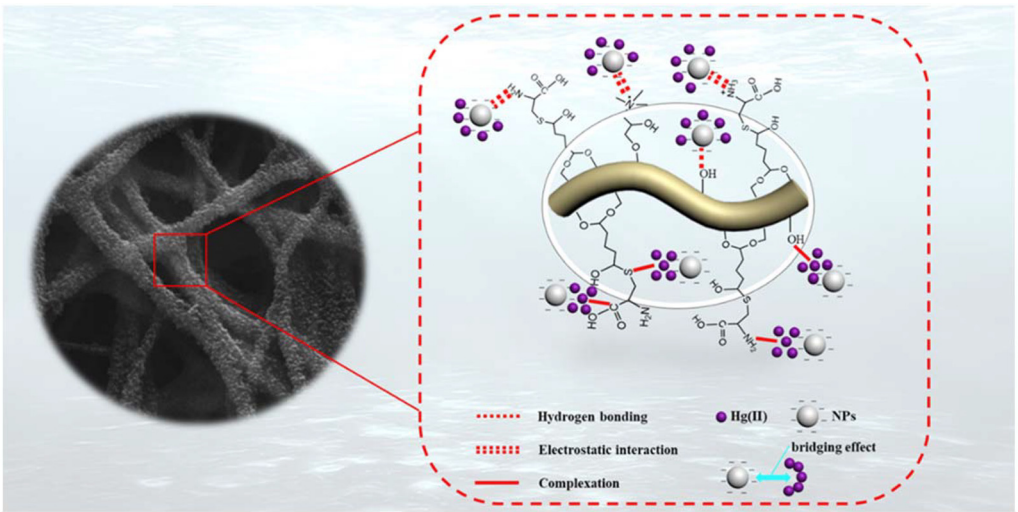

Fig. 11 Schematic representation of the bridging effect between Hg^{2+} and NPs.

3.3 Adsorption mechanism

The aim of this study is to elucidate the adsorption mechanism by characterizing pollutant interactions at the adsorbent's surface. Identifying the critical factors that control adsorption will guide the rational design of materials for improved removal efficiency. The full XPS spectra of the DCAF-GTA-Cys, DCAF-GTA-Cys-NPs, DCAF-GTA-Cys-Hg^{2+}, and DCAF-GTA-Cys-NPs & Hg^{2+} were presented in Fig. S3. High-resolution XPS analysis was performed to confirm the surface modification. As shown in the deconvoluted C 1s spectrum (Fig. 12a), peaks centered at 284.8 eV, 286.4 eV, and 287.8 eV are assigned to C–C, C–O/C–N, and C═O bonds, respectively.[41] The N 1s spectrum (Fig. 12b) exhibits two components at 399.5 eV and 402.2 eV, corresponding to $-NH_2$ and protonated amine ($\equiv N^+$) groups,[42] respectively. Similarly, the O 1s spectrum (Fig. 12c) was resolved into peaks for C═O (531.6 eV), O–H (532.8 eV), and C–O (533.9 eV) bonds.[43] Furthermore, the S 2p spectrum (Fig. 12d) displays the characteristic spin–orbit doublet with S 2p3/2 at 163.3 eV and S 2p1/2 at 164.5 eV.[44] The presence and assignment of these peaks collectively verify the successful modification of the cellulose nanofiber membrane with GTA and L-Cys.

Following NPs adsorption, the C 1s spectrum of DCAF-GTA-Cys-NPs shows an increase in the intensity of the C═O band, implying the successful capture of the NPs. The N 1s peaks shift from 399.5 eV and 402.2 eV to 399.9 eV and 403.3 eV, indicating that $-NH_2$ and $\equiv N^+$ sites interact with NPs through hydrogen bonding and electrostatic interaction. Additionally, the O 1s spectral component corresponding to O–H shifted from 532.8 eV to 533.1 eV. This increase in binding energy indicates that the hydroxyl groups are involved in hydrogen bonding with the carboxyl groups on the NPs. The S 2p peaks remain unchanged, implying no involvement in NPs adsorption. Thus, DCAF-GTA-Cys facilitates NPs adsorption primarily through electrostatic interaction and hydrogen bonding between the adsorbate and the adsorbent.

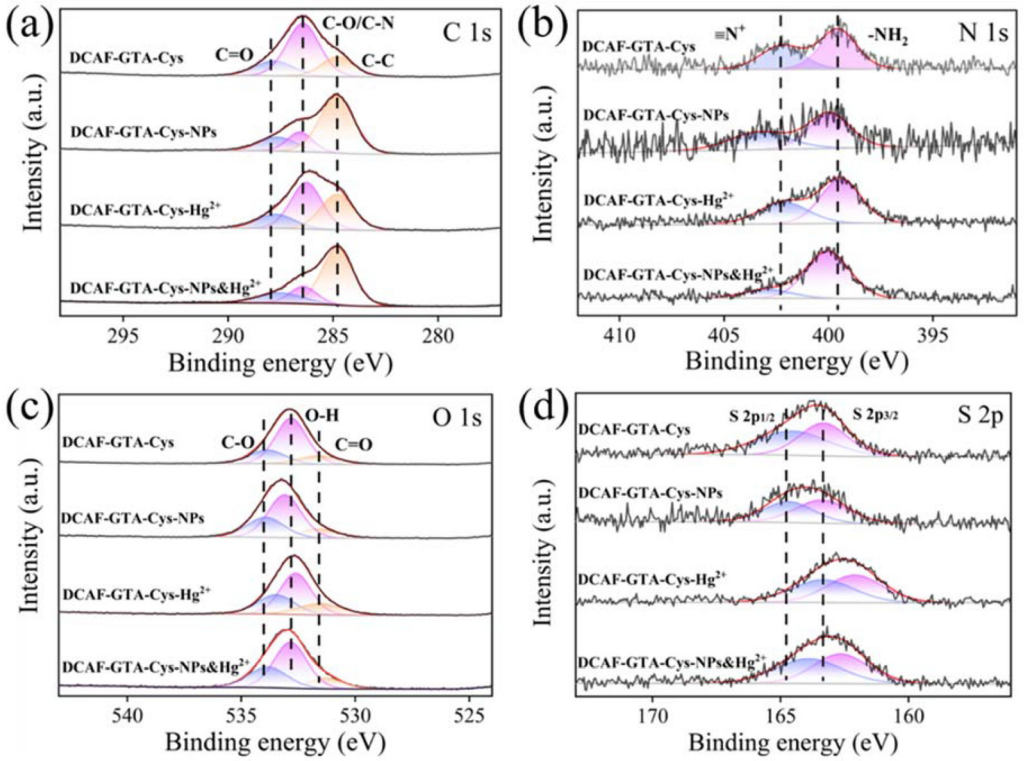

Fig. 12 High resolution spectra of C 1s (a), N 1s (b), O 1s (c) and S 2p (d) of DCAF-GTA-Cys, DCAF-GTA-Cys-NPs, DCAF-GTA-Cys-Hg^{2+} and DCAF-GTA-Cys-NPs & Hg^{2+}.

Upon the adsorption of Hg^{2+}, the observation of Hg 4d and Hg 4f peaks in the full-scan spectrum (Fig. S3) of DCAF-GTA-Cys-Hg^{2+} provides evidence for the effective capture of the heavy metal. Slight negative shifts were observed in the binding energies of the C–O and C═O peaks within the C 1s spectrum, moving from 286.4 eV to 286.3 eV and from 287.8 eV to 287.6 eV, respectively. This shift suggests that both C═O and C–O bonds are involved in the interaction with Hg^{2+}. Additionally, a decrease in the binding energy of $-NH_2$ in the N 1s spectrum from 399.5 eV to 399.4 eV indicates its participation in the reaction with Hg^{2+}.[45] The binding energies for the C═O, O–H, and C–O bonds in the O 1s spectrum also negatively shifted, indicating that these oxygen-containing functional groups in DCAF-GTA-Cys are engaged in the Hg^{2+} adsorption process.[46,47] The observed decrease in the S 2p3/2 and S 2p1/2 binding energies, from 163.3 eV and 164.5 eV to 162.1 eV and 163.3 eV, respectively, provides evidence for a direct interaction between Hg^{2+} and the sulfur atom within the C–S–C bond.[48] Therefore, the adsorption of Hg^{2+} on DCAF-GTA-Cys is facilitated by the complexation of various functional groups, including C–S–C, $-NH_2$, –COOH, and hydroxyl groups, which interact with Hg^{2+}. The specific binding interactions of amino and carboxyl groups with Hg^{2+} are summarized as follows:[49]

$$2(-NH_2) + Hg^{2+} \rightarrow (-NH)_2{-}Hg + 2H^+$$

$$2(COOH) + Hg^{2+} \rightarrow (-COO)_2{-}Hg + 2H^+$$

After the simultaneous adsorption of NPs and Hg^{2+} by DCAF-GTA-Cys, the binding energy of C═O in the C 1s spectrum shifted from 287.8 eV to 287.5 eV, suggesting that the carboxyl groups from the nanofiber surface and the NPs enhance the adsorption of pollutants during the simultaneous adsorption. The negative shift in the C═O peak binding energy to 531.3 eV in the O 1s spectrum further corroborates the above result. Additionally, the binding energies of the N 1s peaks changed from 399.5 eV and 402.2 eV to 399.9 eV and 402.9 eV, while the S 2p3/2 and S 2p1/2 binding energies shifted from 163.3 eV and 164.5 eV to 162.7 eV and 163.9 eV, respectively. These changes indicate that $-NH_2$ and $\equiv N^+$ groups remain as binding sites for NPs, and C–S–C groups continue to interact with Hg^{2+}.[50] Because of the weak interaction between Hg^{2+} and the carboxyl group on the NPs, both Hg^{2+} and NPs could act as bridges, creating a synergistic effect where the presence of each enhances the adsorption of the other.

To gain a deeper understanding of the specific binding sites of the DCAF-GTA-Cys, we performed theoretical calculations of the adsorption process (Fig. 13). Fig. 13a–d illustrate the potential adsorption sites on DCAF-GTA-Cys for NPs. The results show binding energies of −0.87 eV for $\equiv N^+$, −0.53 eV for $-NH_2$, −0.41 eV for C–S–C, and −0.20 eV for –COOH. Given that more negative binding energies indicate a stronger affinity,[51,52] these results suggest that $\equiv N^+$ plays a dominant role in the adsorption of NPs. Fig. 13e–h depict the binding energy calculations for Hg^{2+} at the same functional groups.

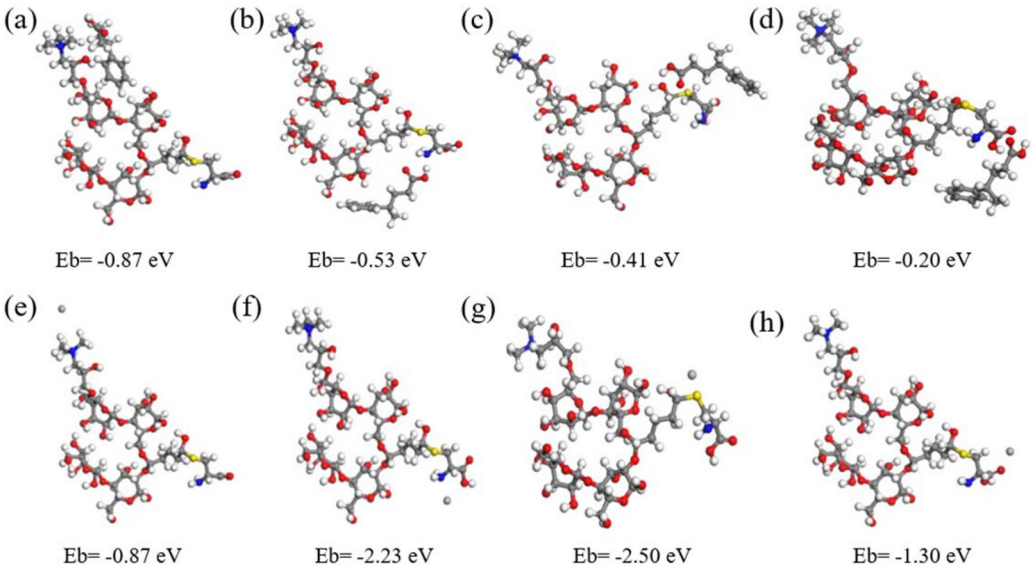

Fig. 13 Adsorption conformations of (a) $\equiv N^+$, (b) $-NH_2$, (c) C–S–C, and (d) –COOH on NPs for DCAF-GTA-Cys. Adsorption conformations of (e) $\equiv N^+$, (f) $-NH_2$, (g) C–S–C, and (h) –COOH on Hg^{2+} for DCAF-GTA-Cys.

The binding energies for $\equiv N^+$, $-NH_2$, C–S–C, and –COOH were −0.87 eV, −2.23 eV, −2.50 eV, and −1.30 eV, respectively. These values suggest notable interactions between Hg^{2+} and $-NH_2$, C–S–C, and –COOH, which is consistent with our XPS analysis. Notably, the largest (most negative) binding energy for Hg^{2+} was observed with C–S–C, confirming that C–S–C is the most effective chelating site for Hg^{2+}, as intended in our design.

4 Conclusion

In summary, we successfully developed a bifunctional cellulose nanofibrous adsorbent, DCAF-GTA-Cys, through a sequential grafting strategy with GTA and L-Cys. This is the first report showing sustainable nanofiber material for concurrent removal of diverse pollutants (specifically encompassing NPs) in complex, co-pollutant scenarios. Characterization confirmed the desired functional groups and structural properties, including enhanced hydrophilicity and mechanical strength suitable for application. The material exhibited moderate adsorption capacities for both NPs (47.6 mg g^{-1}) and Hg^{2+} (65.2 mg g^{-1}) *via* spontaneous and endothermic chemisorption processes following Langmuir monolayer behavior. Mechanistic studies (XPS, DFT) confirmed the specific roles of quaternary ammonium groups for NPs binding and C–S–C/amine/carboxyl groups for Hg^{2+} chelation, with C–S–C sites being particularly effective as designed. Unique bridging interactions between Hg^{2+} and NPs enabled mutual adsorption enhancement, with Hg^{2+} acting as a linker for NPs deposition and NPs serving as platforms for Hg^{2+} chelation. These results demonstrate the potential of DCAF-GTA-Cys as an efficient, multifunctional adsorbent for water remediation. This work represents a promising advancement in the development of environmentally friendly, cost-effective materials for advanced water purification, particularly for tackling the complexities of real-world wastewater containing multiple hazardous contaminants, and highlights the potential for harnessing synergistic effects to boost remediation performance.

Conflicts of interest

There are no conflicts to declare.

Data availability

The data supporting this article have been included as part of the supplementary information (SI). Supplementary information is available. See DOI: https://doi.org/10.1039/d6lp00158k.

Acknowledgements

This work was supported by the Open Research Fund of State Key Laboratory of Polymer Physics and Chemistry, Changchun Institute of Applied Chemistry, Chinese Academy of Sciences (No. 2022-11) and the Fundamental Research Funds for the Central Universities (No. 201912024).

References

1 U. A. Khan, P. Löffler, F. Spilsbury, K. Wiberg, C. S. Lundborg and F. Y. Lai, *J. Hazard. Mater.*, 2024, **480**, 136175.
2 H. Xiao, Z. Zhang, S. Feng, X. Wang and L. Wu, *J. Mater. Chem. A*, 2024, **12**, 31059–31073.

3 M. Urso, M. Ussia and M. Pumera, *Nat. Rev. Bioeng.*, 2023, **1**, 236–251.
4 T. Münzel, O. Hahad, J. Lelieveld, M. Aschner, M. J. Nieuwenhuijsen, P. J. Landrigan and A. Daiber, *Nat. Rev. Cardiol.*, 2024, **22**, 71–89.
5 L. B. Chu and J. L. Wang, *Chem. Eng. J.*, 2023, **468**, 143821.
6 P. Chaturvedi, P. Shukla, B. S. Giri, P. Chowdhary, R. Chandra, P. Gupta and A. Pandey, *Environ. Res.*, 2021, **194**, 110664.
7 Shivangi, S. Bhardwaj and T. Sarkar, *Int. J. Environ. Sci. Technol.*, 2022, **19**, 5595–5610.
8 J. Teng, H. Yu, Z. Liu, L. Bai and Z. Liu, *J. Environ. Chem. Eng.*, 2024, **12**, 114094.
9 H. Sun, B. Yang, Q. Li, X. Zhu, E. Song, C. Liu, Y. Song and G. Jiang, *Nat. Nanotechnol.*, 2024, **19**, 1354–1365.
10 X. Peng, M. Urso, M. Kolackova, D. Huska and M. Pumera, *Adv. Funct. Mater.*, 2024, **34**, 2307477.
11 L. Fusco, A. Gazzi, L. Giro, R. B. Schefer, S. M. D'Almeida, R. Cagliani, M. Zoccheddu, R. Uyar, Ö. Besbinar, D. Çelik, A. Yilmazer, D. M. Mitrano, M. Orecchioni and L. G. Delogu, *Adv. Mater.*, 2024, **37**, 2413413.
12 Y. Wang, M. Wang, Q. Wang, T. Wang, Z. Zhou, M. Mehling, T. Guo, H. Zou, X. Xiao, Y. He, X. Wang, O. J. Rojas and J. Guo, *Adv. Mater.*, 2023, **35**, 2301531.
13 A. Alijagic, O. Kotlyar, M. Larsson, S. Salihovic, A. Hedbrant, U. Eriksson, P. Karlsson, A. Persson, N. Scherbak, K. Färnlund, M. Engwall and E. Särndahl, *Environ. Int.*, 2024, **183**, 108412.
14 J. Zhao, R. Lan, Z. Wang, W. Su, D. Song, R. Xue, Z. Liu, X. Liu, Y. Dai, T. Yue and B. Xing, *Nat. Nanotechnol.*, 2024, **19**, 406–414.
15 Y. Wang, W. Yao, Z. Li, H. Tan, C. Sun, D. Zheng and Y. Zhang, *Int. J. Biol. Macromol.*, 2024, **282**, 137316.
16 T. B. Hofstetter, R. Bakkour, D. Buchner, H. Eisenmann, A. Fischer, M. Gehre, S. B. Haderlein, P. Höhener, D. Hunkeler, G. Imfeld, M. A. Jochmann, S. Kümmel, P. R. Martin, S. G. Pati, T. C. Schmidt, C. Vogt and M. Elsner, *Nat. Water*, 2024, **2**, 14–30.
17 J. Lubchenco, E. F. Camp, C. A. Vargas, D. Belhabib, Z. Anna, D. J. Amon, A. Metaxas and H. Harden-Davies, *Nat. Ecol. Evol.*, 2023, **7**, 1564–1569.
18 H. Zeng, L. Wang, D. Zhang, P. Yan, J. Nie, V. K. Sharma and C. Wang, *Chem. Eng. J.*, 2019, **358**, 253–263.
19 B. Wang, W. Zhang, Y. Zhong, Y. Guo, X. Wang and X. Zhang, *Int. J. Biol. Macromol.*, 2024, **281**, 136427.
20 C. Jeon, K. L. Solis, H.-R. An, Y. Hong, A. D. Igalavithana and Y. S. Ok, *J. Hazard. Mater.*, 2020, **388**, 122048.
21 C. Ji, Y. Ren, H. Yu, M. Hua, L. Lv and W. Zhang, *Chem. Eng. J.*, 2022, **430**, 132960.
22 A. Batool and S. Valiyaveettil, *J. Hazard. Mater.*, 2021, **413**, 125301.
23 H. Zhao, X. Huang, L. Wang, X. Zhao, F. Yan, Y. Yang, G. Li, P. Gao and P. Ji, *Chem. Eng. J.*, 2022, **430**, 133122.
24 S. Peng, X. Chen, X. Rong, H. Ma, C. Zhao and K. Pang, *J. Clean. Prod.*, 2023, **400**, 136708.
25 C. Sun, Z. Wang, H. Zheng, L. Chen and F. Li, *J. Hazard. Mater.*, 2021, **420**, 126599.
26 M. Zheng, K. Xuan, S. Yan, Y. Guo, Y. Huang, R. Xu, K. Zhao, Z. Li, X. Li, H. Jiang and Y. Guo, *Sep. Purif. Technol.*, 2024, **339**, 126550.
27 X. Wang, J. Song, X. Mao, N. Zhao, Y. Zhou and G. Shen, *J. Environ. Chem. Eng.*, 2025, **13**, 117530.
28 H. H. Zhao, Y. Yang, F. M. Song, F. Yan, Y. Yang, P. C. Gao and P. H. Ji, *J. Clean. Prod.*, 2022, **368**, 133124.
29 J. Xue, T. Wu, Y. Dai and Y. Xia, *Chem. Rev.*, 2019, **119**, 5298–5415.
30 K. Zhang, Z. J. Li, W. M. Kang, N. P. Deng, J. Yan, J. G. Ju, Y. Liu and B. W. Cheng, *Carbohydr. Polym.*, 2018, **183**, 62–69.
31 X. Wu, Z. Wang, G. Shao, B. Qin, Y. Wang, T. Wang, Z. Liu and Y. Fu, *React. Funct. Polym.*, 2024, **194**, 105759.
32 W. Li, B. Ju and S. Zhang, *RSC Adv.*, 2019, **9**, 6986–6994.
33 A. Kayan, *J. Appl. Polym. Sci.*, 2012, **123**, 3527–3534.
34 A. Kayan, *J. Inorg. Organomet. Polym. Mater.*, 2016, **26**, 640–647.
35 N. Ballav, R. Das, S. Giri, A. M. Muliwa, K. Pillay and A. Maity, *Chem. Eng. J.*, 2018, **345**, 621–630.
36 X. Huang, L. Wang, J. B. Zhang, X. J. Du, S. J. Wu, H. X. Wang and X. L. Wei, *Int. J. Biol. Macromol.*, 2020, **163**, 1915–1925.
37 H. Li, Y. Duan, Y. Shao, Z. Zhang and L. Ren, *J. Mater. Chem. A*, 2024, **12**, 14885–14939.
38 R. Ezzati, *Chem. Eng. J.*, 2020, **392**, 123705.
39 T. Li, X. Du, X. Wang, Y. Zhou, J. Li, M. Wang and L. Zhou, *Chem. Eng. J.*, 2024, **500**, 157176.
40 Y. Y. Zhang, Y. Y. Luo, X. Q. Yu, D. F. Huang, X. T. Guo and L. Y. Zhu, *Water Res.*, 2022, **219**, 118544.
41 G. V. Demirci, M. T. Baig and A. Kayan, *Int. J. Biol. Macromol.*, 2024, **283**, 137950.
42 X. Y. Lin, D. T. Tran, M. H. Song and Y. S. Yun, *J. Hazard. Mater.*, 2022, **422**, 126940.
43 J. Zhuang, N. N. Rong, X. R. Wang, C. C. Chen and Z. Y. Xu, *Sep. Purif. Technol.*, 2022, **293**, 121133.
44 T. Z. Yin, Y. S. Zhang, D. Dong, T. Wang and J. W. Wang, *J. Clean. Prod.*, 2022, **355**, 131814–131825.
45 H. H. Zeng, L. Wang, D. Zhang and C. Y. Wang, *Chem. Eng. J.*, 2023, **468**, 143621.
46 K. Wu, B. Wang, T. Liu, J. Wang, W. Xu, B. Zhang and Y. Niu, *Int. J. Biol. Macromol.*, 2023, **253**, 126590.
47 L. Lang, B. Wang, T. Liu, J. Wang, L. Zhu, Y. Liu and Y. Niu, *Chem. Eng. J.*, 2023, **477**, 147310.
48 J. W. Chen, M. L. Yuan, W. Q. Cai, J. H. Wei, J. P. Zhou, P. Liu, Z. C. Yang, J. L. Luo, Q. Xia and Z. J. Cai, *Chem. Eng. J.*, 2021, **422**, 130153.
49 S. Kushwaha, B. Sreedhar and P. P. Sudhakar, *Chem. Eng. J.*, 2012, **193**, 328–338.
50 Y. Zhou, X. Zhou, S. Hu, H. Wu, J. Ren and F. Yue, *Ind. Crops Prod.*, 2024, **222**, 120026.
51 J. H. Sun, X. X. Zhao, R. M. Hu, G. X. Sun, H. Zhao, W. S. Liu, Z. S. Bai, X. C. Jiang and Y. Cui, *Int. J. Biol. Macromol.*, 2023, **253**, 127110.
52 P. P. Zhang, Y. Y. Yang, X. G. Duan, Y. J. Liu and S. B. Wang, *ACS Catal.*, 2021, **11**, 11129–11159.